Resonance crossing of a charged body in a magnetized Kerr background: An analog of extreme mass ratio inspiral

Sajal Mukherjee[1,*] Ondřej Kopáček[1,2,†] and Georgios Lukes-Gerakopoulos[1,‡]

[1]*Astronomical Institute of the Czech Academy of Sciences,*
Boční II 1401/1a, CZ-141 00 Prague, Czech Republic
[2]*Faculty of Science, Humanities and Education, Technical University of Liberec,*
Studentská 1402/2, CZ-461 17 Liberec, Czech Republic

We investigate resonance crossings of a charged body moving around a Kerr black hole immersed in an external homogeneous magnetic field. This system can serve as an electromagnetic analog of a weakly nonintegrable extreme mass ratio inspiral (EMRI). In particular, the presence of the magnetic field renders the conservative part of the system nonintegrable in the Liouville sense, while the electromagnetic self-force causes the charged body to inspiral. By studying the system without the self-force, we show the existence of an approximate Carter-like constant and discuss how resonances grow as a function of the perturbation parameter. Then, we apply the electromagnetic self-force to investigate crossings of these resonances during an inspiral. Averaging the energy and angular momentum losses during crossings allows us to employ an adiabatic approximation for them. We demonstrate that such adiabatic approximation provides results qualitatively equivalent to the instantaneous self-force evolution, which indicates that the adiabatic approximation may describe the resonance crossing with sufficiently accuracy in EMRIs.

DOI: 10.1103/PhysRevD.107.064005

I. INTRODUCTION

Dynamical systems under nonintegrable perturbation exhibit various extraordinary features compared to the unperturbed ones [1]. First of all, the perturbation may trigger chaotic motions in some regions of the phase space. Depending on the strength of the perturbation, deterministic chaos may completely dominate the dynamics. However, even in the slightly perturbed systems with negligible amount of chaos, we observe dynamically relevant nonintegrable effects near resonances, i.e., in parts of the phase space, where the characteristic frequencies of the system are commensurate. In fact, according to the *Kolmogorov-Arnold-Moser* (KAM) theorem [2], parts of the phase space of a weakly perturbed system that are far enough from resonances remain basically unaffected by the imposed perturbation. On the other hand, the dynamics in the vicinity of resonances considerably differs which may affect measurable properties of the system. Motivated by the latter fact, there were studies trying to provide some insight into the dynamics of an extreme mass ratio inspiral (EMRI) crossing the resonance [3–8].

EMRIs represent a key observational target for the future mission of Laser Interferometer Space Antenna (LISA) [9].

They are composed of a supermassive primary black hole and a much lighter secondary compact object (black hole or neutron star) inspiralling into the primary. The mass ratio $\eta = m/M$ between the mass m of the secondary to the mass M of the primary is smaller than 10^{-4}. The smallness of η allows us to use it as a perturbation parameter when expanding the background spacetime of this binary system in orders of η to calculate the gravitational self-force (GSF) [10,11]. Actually, the dissipative part of this self-force causes the secondary to inspiral towards the primary as it radiates away energy and angular momentum in the form of gravitational waves.

The full first order self-force for a nonspinning secondary moving on a generic orbit has been obtained relatively recently [11,12], but using the full self-force is computationally expensive. The main cause is that the inspiralling body revolves around the primary body for a number of cycles inversely proportional to the mass ratio of the system (η^{-1}). Since the mass ratio in an EMRI is small, the number of cycles becomes very large making the numeric computations highly demanding. In order to decrease the computational demands, the gravitational self-force may be approximated in some way. In particular, we may employ an adiabatic approximation [13], which takes into account just the averaged dissipative part of the first order self-force, while more advanced approximations are also available [14,15].

Actually, Ref. [14] attempts to tackle the issue that during the many EMRI cycles, it is almost certain that the

*mukherjee@asu.cas.cz
†kopacek@asu.cas.cz
‡gglukes@gmail.com

inspiralling body will cross resonances, i.e., some of the orbital characteristic frequencies of the secondary will become commensurate [3,16–19]. Not all of these crossings are equally important. Only those with a small denominator, like 1:2, 2:3, are expected to have a significant impact on the inspiral [20]. It has not yet been clarified up to which value of the denominator we should expect this impact, but we speculate that it should be a value of the order of 10. Most of the models we use to approximate an EMRI are problematic at the resonances [20]; however, as was already mentioned there is an ongoing effort to overcome this obstacle [7,14] and this work is part of this effort.

Mutual effects of the electromagnetic and the gravitational self-force in the dynamics of a charged compact body has recently been studied in the context of EMRIs [21]. That study has shown that besides the interaction terms previously derived in [22], additional perturbative terms linear in the metric perturbation are generated and these terms may become relevant in some astrophysical situations. However, here we adopt a different approach and we do not consider combined effects of the both interactions. In our scenario, the electromagnetic self-force exerted on the charged body in a magnetized spacetime serves as an analog model of a gravitational self-force [23] which we, however, do not consider explicitly. Although, the evolution of an EMRI system and the emission of the gravitational radiation are actually governed by the gravitational self-force, here we deal with the aspects of the dynamics correlated with the resonances and their crossing due to dissipation within the electromagnetic analog framework, which allows us to avoid the intricate formalism of the gravitational self-force [24,25].

The primary motivation of this work is to study the system with the electromagnetic self-force as an analog of an EMRI, however, the fact that we study dynamics of an electrically charged body in the vicinity of a magnetized rotating black hole, makes the results of our analysis relevant also to other astrophysical applications. Hence, let us discuss a little bit the framework of this model. We consider an asymptotically uniform magnetic field aligned with the rotation axis of the black hole described by a vacuum model derived by Wald in [26]. Albeit asymptotically uniform, the field becomes largely deformed due to frame dragging and other relativistic effects if we get closer to the horizon of the black hole [27,28]. Although the employed weak-field approximation does not take into account the effect of the field onto the curvature of the spacetime, the geometric effects of the spinning black hole onto the topology of the electromagnetic field are described completely by the given model.

On the other hand, the effect of the charged matter onto the electromagnetic field is neglected in this framework. This might appear as an issue especially within the inner parts of the accretion disk where the presence of charges

and currents significantly contributes to the field and, in particular, small-scale magnetic fields may be induced here due to turbulence driven by the magnetorotational instability [29]. Turbulence allows the transport of the angular momentum and, thus, contributes to the viscosity of the disk which is crucial for the accretion process. Nevertheless, for the study of the resonance crossing, the small-scale structure of the magnetic field and full description of the physics of accretion is not relevant. In fact, the organized large-scale field [26] provides an appropriate framework allowing the dissipation of the energy and angular momentum due to radiation losses of the charged test body [30].

The model of an axisymmetric vacuum magnetosphere of the rotating black hole described by the Wald's solution [26] of the Maxwell's equations on the Kerr background has been employed in various contexts. For instance, it has been shown that this model (unlike the pure Kerr or Kerr-Newman background) allows stable off-equatorial circular orbits [31], which are astrophysically relevant as a basic model to study the dynamics of diluted plasma in an accretion disk coronae. Moreover, the magnetic field acts as a nonintegrable perturbation triggering (deterministic) chaos in some regions of the phase space [32] and chaotic dynamics may contribute to launching the outflow of escaping jetlike trajectories [33–35]. Hence, although, the model of vacuum magnetosphere does not attempt to provide a complete description of the field topology of an accreting black hole, it represents an useful approximation which allows the study of various astrophysically relevant processes.

The rest of the article is organized as follows. Section II introduces the system of a charged body moving in a Kerr background with a test external magnetic field without self-force. Section III discusses how a resonances grow in this system. Section IV studies the crossings of resonances when the dissipation due to instantaneous electromagnetic self-force is imposed, while Sec. V compares the instantaneous self-force results with the adiabatic ones. Finally, Sec. VI examines our parameter choices and Sec. VII discusses our main findings.

II. MOTION OF A CHARGED BODY IN AN EXTERNAL ELECTROMAGNETIC FIELD

In this section, we discuss the motion of a charged body around a magnetized Kerr black hole without the electromagnetic self-force. We start with the equations of motion and the conserved quantities, and then we discuss the integrability of the system and the existence of a Carter-like constant.

A. Equations of motion

The equations of motion for a charged body in a curved background read

$$\frac{DU^\mu}{d\tau} = \tilde{q}F^\mu{}_\nu U^\nu, \tag{1}$$

where, 'D' denotes a covariant derivative, τ is the proper time, $\tilde{q} = q/m$ denotes the specific charge of a body with rest mass m, U is the 4-velocity, and $F_{\mu\nu}$ is the electromagnetic field tensor.

The equations of motion (1) actually represent a set of second-order differential equations in Boyer-Lindquist coordinates $x^\mu = (t, r, \theta, \phi)$. However, one can employ the Hamiltonian formalism to obtain equivalent set of first order equations for the canonical coordinates (x^μ, π_ν), where $\pi_\nu = (\pi_t, \pi_r, \pi_\theta, \pi_\phi)$ are components of the canonical four-momentum. The Hamiltonian of a body with electric charge q and rest mass m in a vector potential field A_μ can be defined as [36]

$$H = \frac{1}{2}g^{\mu\nu}(\pi_\mu - qA_\mu)(\pi_\nu - qA_\nu), \tag{2}$$

where $g_{\mu\nu}$ is the metric of the background spacetime. The vector potential A_μ is related to the electromagnetic field tensor as $F_{\mu\nu} = \partial_\mu A_\nu - \partial_\nu A_\mu$.

The equations of motion are

$$\frac{dx^\mu}{d\lambda} \equiv P^\mu = \frac{\partial H}{\partial \pi_\mu}, \qquad \frac{d\pi_\mu}{d\lambda} = -\frac{\partial H}{\partial x^\mu}, \tag{3}$$

where $\lambda \equiv \tau/m$ is a dimensionless affine parameter. By employing the first equation we obtain the kinematical four-momentum $P^\mu = \pi^\mu - qA^\mu$, and the conserved value of the Hamiltonian is therefore $H = -m^2/2$.

B. Kerr spacetime

Within this study we consider a fixed spacetime background of a rotating black hole. The line element of the Kerr metric in Boyer-Lindquist coordinates reads

$$ds^2 = g_{tt}dt^2 + 2g_{t\phi}dtd\phi + g_{\phi\phi}d\phi^2 + g_{rr}dr^2 + g_{\theta\theta}d\theta^2, \tag{4}$$

where

$$g_{tt} = -\left(1 - \frac{2Mr}{\Sigma}\right), \qquad g_{t\phi} = -\frac{2aMr\sin^2\theta}{\Sigma},$$

$$g_{\phi\phi} = \frac{(\varpi^4 - a^2\Delta\sin^2\theta)\sin^2\theta}{\Sigma}, \qquad g_{rr} = \frac{\Sigma}{\Delta},$$

$$g_{\theta\theta} = \Sigma, \tag{5}$$

with

$$\Sigma = r^2 + a^2\cos^2\theta, \quad \Delta = \varpi^2 - 2Mr, \quad \varpi^2 = r^2 + a^2, \tag{6}$$

where M is the mass of the black hole and a is the Kerr spin parameter.

C. Asymptotically uniform magnetic field

We employ a simple model of a vacuum magnetosphere consisting of an asymptotically uniform magnetic field aligned with the spin of the black hole. The relevant test-field solution of Maxwell's equations on the Kerr background may be derived exploiting the fact that in this case the Killing vectors themselves, as well as their linear combinations, solve the Maxwell's equation [26]. In particular, the vector potential $A_\mu = (A_t, 0, 0, A_\phi)$ of the solution corresponding to the magnetic field of the asymptotic strength B_0 may be expressed in terms of covariant components of the Kerr metric tensor $g_{\mu\nu}$ as follows:

$$A_t = \frac{B_0}{2}(g_{t\phi} + 2ag_{tt}), \qquad A_\phi = \frac{B_0}{2}(g_{\phi\phi} + 2ag_{t\phi}). \tag{7}$$

Since the vector potential of a stationary axisymmetric field does not depend on the coordinates t and ϕ, we obtain the following set of nonzero components of the electromagnetic field tensor:

$$F_{\theta t} = -F_{t\theta} = \frac{2B_0 Mar\tilde{x}\tilde{y}(a^2 - r^2)}{\Sigma^2}, \tag{8}$$

$$F_{rt} = -F_{tr} = \frac{B_0 Ma(\tilde{x}^2 - 2)(r^2 - a^2\tilde{y}^2)}{\Sigma^2}, \tag{9}$$

$$\begin{aligned}
F_{r\phi} &= -F_{\phi r} \\
&= \frac{B_0\tilde{x}^2}{\Sigma^2}(a^4 r\tilde{x}^4 - 2a^4 r\tilde{x}^2 + a^4 r - Ma^4\tilde{x}^4 \\
&\quad + 3Ma^4\tilde{x}^2 - 2Ma^4 - 2a^2 r^3\tilde{x}^2 + 2a^2 r^3 \\
&\quad - Ma^2 r^2\tilde{x}^2 + 2Ma^2 r^2 + r^5),
\end{aligned} \tag{10}$$

$$\begin{aligned}
F_{\theta\phi} &= -F_{\phi\theta} \\
&= \frac{B_0\tilde{y}\tilde{x}}{\Sigma^2}(a^6\tilde{y}^4 + a^4 r^2\tilde{y}^4 + 2a^4 r^2\tilde{y}^2 \\
&\quad - 2Ma^4 r\tilde{y}^4 - 2Ma^4 r + 2a^2 r^4\tilde{y}^2 + a^2 r^4 \\
&\quad - 4Ma^2 r^3\tilde{y}^2 + r^6),
\end{aligned} \tag{11}$$

where we set $\tilde{x} \equiv \sin\theta$ and $\tilde{y} \equiv \cos\theta$.

We consider the model of a *weakly-magnetized* black hole, in which the contribution of the electromagnetic field to the stress-energy tensor $T^{\mu\nu}$ is neglected and the field, thus, does not affect the spacetime geometry nor the motion of electrically neutral bodies. Using such test-field approximations is justified in astrophysical conditions, while the relevant field intensities encountered in cosmic environments are too low to affect the geometry significantly even in extreme cases of neutron stars and magnetars [37].

Even if the field given by Eq. (7) is asymptotically uniform, in the vicinity of a rotating black hole the field structure becomes distorted by the frame-dragging and other effects of strong gravity [e.g., [28]]. In particular, the

horizon of the Kerr black hole tends to expel the magnetic field as the spin increases. With the extreme rotation ($a = M$), the expulsion becomes complete and the invariant magnetic flux through each hemisphere of the horizon drops to zero in what is known as black hole Meissner effect [27,38,39]. While this effect only operates in an axisymmetric field [40], other remarkable effects like the emergence of magnetic null points may arise in non-axisymmetric vacuum magnetospheres of black holes or neutron stars [41,42]. Nevertheless, in the present paper we restrict the discussion to the perfectly axisymmetric model of Kerr black hole immersed into a weak asymptotically uniform magnetic field aligned with the spin axis described by Eq. (7).

D. Conserved quantities

In this section, we consider the system without the electromagnetic self-force. Therefore, the value of the Hamiltonian given by Eq. (2) remains conserved as $H = -m^2/2$. Due to the stationarity and the axisymmetry of the system, the relevant components of the canonical four-momentum π_t and π_ϕ are also conserved and define the integrals E (energy) and L_z (axial component of the angular momentum) as follows:

$$-E \equiv \pi_t = P_t + qA_t, \qquad L_z \equiv \pi_\phi = P_\phi + qA_\phi. \quad (12)$$

In addition to the timelike and spacelike Killing vectors, the Kerr spacetime is also endowed with a Killing tensor. Due to this, once we switch off the magnetic field (or consider electrically neutral bodies which are not affected by the weak field), we find the fourth conserved quantity, namely the Carter constant [43]. The existence of four independent and in involution integrals of motion in a system of four degrees of freedom assures full Liouville integrability of the system [1].

Below we discuss the existence of a Carter-like constant in the presence of the external magnetic field. In order to investigate that, we employ the Carter's theorem [44,45]. This theorem assumes an axisymmetric spacetime with metric coefficients which may be expressed as

$$g^{tt} = (\mathcal{T}_{tt} + \Theta_{tt})/(\Sigma_r + \Sigma_\theta), \qquad g^{rr} = \mathcal{T}_{rr}/(\Sigma_r + \Sigma_\theta),$$
$$g^{\theta\theta} = \Theta_{\theta\theta}/(\Sigma_r + \Sigma_\theta), \qquad g^{t\phi} = (\mathcal{T}_{t\phi} + \Theta_{t\phi})/(\Sigma_r + \Sigma_\theta),$$
$$g^{\phi\phi} = (\mathcal{T}_{\phi\phi} + \Theta_{\phi\phi})/(\Sigma_r + \Sigma_\theta), \quad (13)$$

where $\mathcal{T}_{tt}$, $\mathcal{T}_{t\phi}$, $\mathcal{T}_{\phi\phi}$, $\mathcal{T}_{rr}$, and Σ_r are functions that only depend on the radial coordinate r, while Θ_{tt}, $\Theta_{\theta\theta}$, $\Theta_{t\phi}$, $\Theta_{\phi\phi}$, and Σ_θ are functions of θ only. In such spacetime, if we can express a Hamiltonian H_c in the form

$$H_c = \frac{1}{2m}\frac{H_r + H_\theta}{\mathcal{W}_r + \mathcal{W}_\theta}, \quad (14)$$

where H_r and $\mathcal{W}_r$ are functions of r only, and H_θ and $\mathcal{W}_\theta$ are functions of θ only, then the following quantity commutes with the Hamiltonian,

$$\mathcal{K} = 2\mathcal{W}_r H_c - H_r = H_\theta - 2\mathcal{W}_\theta H_c = \frac{\mathcal{W}_r H_\theta - \mathcal{W}_\theta H_r}{\mathcal{W}_r + \mathcal{W}_\theta}. \quad (15)$$

Given that our work concerns the Kerr background, by comparing the expressions in Eq. (13) with the Kerr metric coefficients, we arrive at

$$\mathcal{T}_{tt} = -(r^2 + a^2)^2/\Delta, \qquad \mathcal{T}_{t\phi} = -a(r^2 + a^2)/\Delta,$$
$$\mathcal{T}_{\phi\phi} = -a^2/\Delta \qquad \mathcal{T}_{rr} = \Delta, \qquad \mathcal{T}_{\theta\theta} = 1,$$
$$\Theta_{tt} = a^2\sin^2\theta, \qquad \Theta_{\theta\theta} = 1, \qquad \Theta_{t\phi} = a,$$
$$\Theta_{\phi\phi} = 1/\sin^2\theta, \qquad \Sigma_r = r^2, \qquad \Sigma_\theta = r^2\cos^2\theta. \quad (16)$$

To check if we can write the Hamiltonian (2) in a manner similar to Eq. (14), we first expand it

$$\begin{aligned} 2H &= g^{\mu\nu}P_\mu P_\nu \\ &= g^{tt}(P_t)^2 + 2g^{t\phi}P_t P_\phi + g^{\phi\phi}(P_\phi)^2 \\ &\quad + g^{rr}(P_r)^2 + g^{\theta\theta}(P_\theta)^2. \end{aligned} \quad (17)$$

In the above, the four-momentum is related with the 4-velocity as $P_\mu = m\mathcal{U}_\mu$. Note that P^r and P^θ are arbitrary, while P_t and P_ϕ can be obtained from the relations given in Eq. (12),

$$\begin{aligned} P_t &= -E - (\epsilon/2)(g_{t\phi} + 2ag_{tt}), \\ P_\phi &= L_z - (\epsilon/2)(g_{\phi\phi} + 2ag_{t\phi}), \end{aligned} \quad (18)$$

where $\epsilon = qB_0$ is a key parameter which scales the electromagnetic interaction and introduces the nonintegrable perturbation to the geodesic motion. Note that as we employ the weak-field solution given by Eq. (7), the charge q and the asymptotic magnetic induction B_0 always couple as qB_0 leaving ϵ as the only independent parameter.

Having done the above two steps allow us to rewrite the Hamiltonian as follows:

$$\begin{aligned} 2H &= g^{tt}E^2 + 2g^{t\phi}EL_z + g^{\phi\phi}L_z^2 + g^{rr}(P_r)^2 + g^{\theta\theta}(P_\theta)^2 \\ &\quad + \epsilon E[g^{tt}(g_{t\phi} + 2ag_{tt}) + g^{t\phi}(g_{\phi\phi} + 2ag_{t\phi})] \\ &\quad - \epsilon L_z[g^{\phi\phi}(g_{\phi\phi} + 2ag_{t\phi}) + g^{t\phi}(g_{t\phi} + 2ag_{tt})] \\ &\quad + \epsilon^2 \mathcal{F}, \end{aligned} \quad (19)$$

where we define $\mathcal{F}$ as

$$\mathcal{F} = \frac{1}{4}[g^{tt}(g_{t\phi} + 2ag_{tt})^2 + g^{\phi\phi}(g_{\phi\phi} + 2ag_{t\phi})^2$$
$$+ 2g^{t\phi}(g_{t\phi} + 2ag_{tt})(g_{\phi\phi} + 2ag_{t\phi})]. \quad (20)$$

The Hamiltonian can be written in a more compact form as follows:

$$H = H_0 - \frac{\epsilon}{2}(L_z - 2aE) + \epsilon^2 \mathcal{F} = H_{\text{int}} + \epsilon^2 \mathcal{F}, \quad (21)$$

where H_0 and H_{int} are defined as

$$H_{\text{int}} = H_0 - \frac{\epsilon}{2}(L_z - 2aE), \quad (22)$$

$$H_0 = \frac{1}{2}(g^{tt}E^2 - 2g^{t\phi}EL_z + g^{\phi\phi}L_z^2 + g^{rr}P_r^2 + g^{\theta\theta}P_\theta^2)$$
$$= \frac{1}{2\Sigma}[(\mathcal{T}_{tt}E^2 - 2\mathcal{T}_{t\phi}EL_z + \mathcal{T}_{\phi\phi}L_z^2 + \Delta P_r^2)$$
$$+ (\Theta_{tt}E^2 - 2\Theta_{t\phi}EL_z + \Theta_{\phi\phi}L_z^2 + P_\theta^2)]. \quad (23)$$

In the above, H_0 corresponds to the Hamiltonian for a Kerr geodesic. Interestingly, the linear-order perturbation in ϵ is only introducing an additional constant term to this Hamiltonian, as can be seen from Eq. (21). Therefore, if the Hamiltonian H_0 is separable in r and θ, so should be H_{int}. On the other hand, $\mathcal{F}$ is a coupling term in r and θ, which renders the total Hamiltonian H not separable in these coordinates. Therefore, to be able to employ Carter's theorem, we drop the term $\mathcal{F}$, which linearizes H in ϵ, and work with H_{int}. By using the metric components given in Eq. (13), we can break Eq. (22) into two pieces,

$$H_r^0 = \Delta P_r^2 + \mathcal{T}_{tt}E^2 - 2\mathcal{T}_{t\phi}EL_z + \mathcal{T}_{\phi\phi}L_z^2,$$
$$H_\theta^0 = P_\theta^2 + \Theta_{tt}E^2 - 2\Theta_{t\phi}EL_z + \Theta_{\phi\phi}L_z^2, \quad (24)$$

and the Hamiltonian given in Eq. (21) now reads

$$H_{\text{int}} = \frac{1}{2\Sigma}(H_r^0 + H_\theta^0 - \Sigma H_1)$$
$$= \frac{1}{2\Sigma}(H_r^0 - r^2 H_1 + H_\theta^0 - a^2 \cos^2\theta H_1), \quad (25)$$

where, $H_1 = \epsilon(L_z - 2aE)$. By rewriting the above with $H_r = H_r^0 - r^2 H_1$, and $H_\theta = H_\theta^0 - a^2 \cos^2\theta H_1$, we obtain finally

$$H_{\text{int}} = \frac{1}{2\Sigma}(H_r + H_\theta). \quad (26)$$

Hence, by ignoring the $\mathcal{O}(\epsilon^2)$ term in Eq. (22), there is essentially a constant term added to the unperturbed Hamiltonian H_0, and, therefore, the overall integrability is retained. This is given by the Hamiltonian H_{int}. Below

we present the expression for the Carter-like constant for future references. By using Eq. (15) we get

$$\mathcal{K} = \frac{1}{\Sigma}(r^2 H_\theta - a^2 \cos^2\theta H_r). \quad (27)$$

We have verified that the Poisson bracket between $\mathcal{K}$ and H_{int} identically vanishes, i.e., $\{\mathcal{K}, H_{\text{int}}\} = 0$, while $\{\mathcal{K}, H\} = \mathcal{O}(\epsilon^2)$, as argued before. This serves as a sanity check for the derivation of the Carter-like constant $\mathcal{K}$ in Eq. (27). Note that originally, the quantity $\mathcal{K} - (L_z - aE)^2$ was described as the Carter's constant in Kerr spacetime [43]. However, we will confine ourselves with the definition (27) throughout the rest of the paper. In addition, we will use the notation $\tilde{E} = E/m$, $\tilde{L}_z = L_z/m$, $\tilde{H} = H/m^2$ and $\tilde{\mathcal{K}} = \mathcal{K}/m^2$, to denote specific energy, momentum, Hamiltonian and Carter-like constant respectively. Moreover, we define $\tilde{\epsilon} = \epsilon/m = \tilde{q}B_0$. Finally, we should stress that the linearization of the Hamiltonian is only to introduce the concept of Carter-like constant in the present section. For future references in the paper, we will always use the full Hamiltonian H and not H_{int}.

Recall that unlike gravity, electromagnetism has both repulsive and attractive nature. In our system, assuming $a > 0$ and $q > 0$, the repulsion occurs when the external magnetic field is parallel to L_z component of the angular momentum of the body while the force is attractive when they are antiparallel. We discuss both cases until Sec. IV B; however, then we restrict ourselves on the case of attraction since we study this system as an analog of an EMRI.

III. RESONANCE GROWTH

In the previous section, we have shown that a system of nonradiating charged particle in a magnetized Kerr background preserves its integrability if the terms $\mathcal{O}(\epsilon^2)$ are neglected. Nevertheless, in the rest of paper we consider the full Hamiltonian system (2) and we focus on particular effects, which the nonintegrable perturbation has upon resonances. This section, in particular, discusses how a resonance grows as the perturbation increases, which is achieved by measuring the resonance width w.

The width w of a resonance is formally defined as the difference between the maximum and the minimum values of the action on the separatrix of a pendulum to which a resonance can be approximated to by a normal form (for more details see [7,46]). Here we adapt an approach applied in [7] and we measure this width from rotation curves obtained by the analysis of Poincaré sections. The rest of this section outlines the employed procedure.

A. The resonance in Poincaré section and rotation curve

A resonance occurs when two or more characteristic frequencies of the system are commensurate. In our work,

we are interested in resonances between the polar ω_θ frequency and the radial frequency ω_r. Resonances play an important role when an integrable system, like the geodesic motion on a Kerr background, is perturbed in such way that integrability is lost. According to the KAM theorem [2], the tori of the integrable system that are sufficiently away from a resonance survive the perturbation and are just slightly deformed. On such tori we observe quasiperiodic orbits which are characterized by irrational frequency ratios. On the other hand, the resonant tori in the perturbed system dissolve and only an even number of periodic orbits survive according to the *Poincaré-Birkhoff* theorem [47]; half of these orbits are stable with secondary islands of stability forming around them and the other half unstable with corresponding asymptotic manifolds stemming from them. These orbits form the so-called Birkhoff chain.

A way to investigate the resonance growth is to track them on Poincaré sections for different values of ϵ, while keeping fixed the energy E, the angular momentum L_z and the Kerr parameter a. Practically, in our system a Poincaré section is formed, when we register the momentum π_r and the radial coordinate r in the Hamiltonian flow crossings of the equatorial plane with a specific orientation, e.g., when an orbit crosses the plane with $\pi_\theta > 0$. Spotting a resonance on a Poincaré section just by inspecting it is often quite difficult, see, e.g., the top panel of Fig. 1. To achieve it in a two degrees of freedom system, a useful tool is the rotation number [48,49], which provides the ratio of the characteristic frequencies.

A rotation number can be calculated from a Poincaré section. The first step is to identify a fixed point $\vec{x}_c$ on the Poincaré section, around which closed curves are nested. This point is often called the center of the main island of stability and the curves correspond to cuts through tori, for which the frequency ratio is an irrational number. In the top panel of Fig. 1 the position of the fixed point is marked by a black dot. In the next step, rotation angles between successive intersections $\vec{x}_i$ with the section with respect to $\vec{x}_c$ are calculated as

$$\vartheta_i = \text{ang}[(\vec{x}_{i+1} - \vec{x}_c), (\vec{x}_i - \vec{x}_c)]. \qquad (28)$$

The rotation number is then defined as

$$\nu_\vartheta = \lim_{n \to \infty} \frac{1}{2\pi n} \sum_{i=1}^{n} \vartheta_i. \qquad (29)$$

For finite n the accuracy of the rotation number is of the order of $1/n$. For an integrable nondegenerate Hamiltonian system, the rotation number changes monotonically for initial conditions getting radially further away from $\vec{x}_c$. The respective curve is called rotation curve. When the integrability is broken, then at the resonances the rotation curve fluctuates randomly, when it is calculated on a chaotic
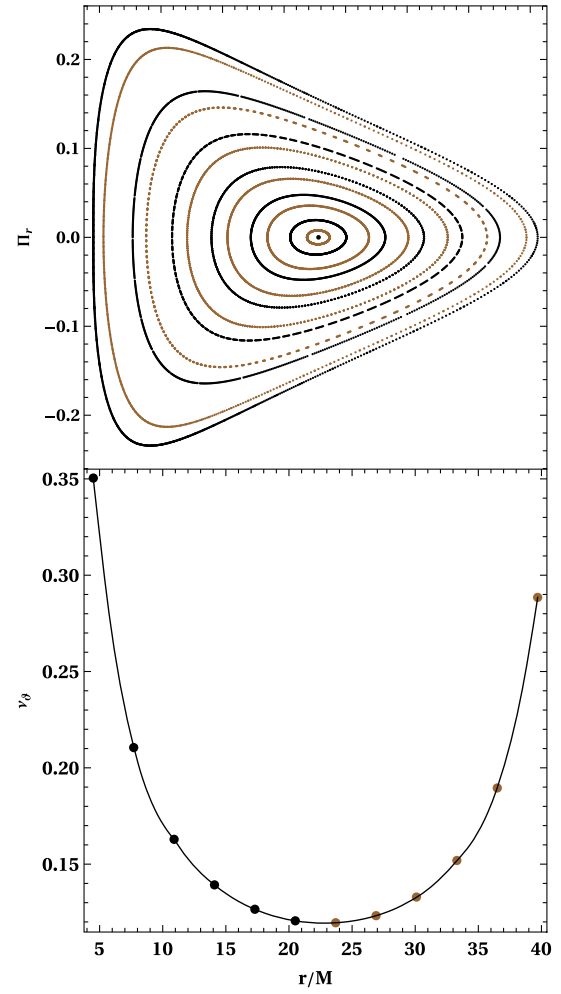

FIG. 1. The top panel shows a Poincaré section for the parameters: $\tilde{E} = 0.98$, $\tilde{L}_z = 3.3M$, and $\tilde{\epsilon} = -10^{-3}M^{-1}$, while the bottom panel shows the respective rotation curve when we take initial conditions along the $\pi_r = 0$ line of the Poincaré section. We show 12 initial conditions along this line starting from $r_i = 4.5M$ and changing the initial distance with a step of $3.2M$. Each point on the rotation curve indicates the respective initial condition for a KAM curve depicted on the Poincaré section. The coloring indicates whether an initial condition lies left (black) or right (brown) from the center of the main island of stability.

layer, or provides a plateau, when it is calculated on a secondary island of stability. The bottom panel of Fig. 1 shows how the rotation curve looks like when we scan the section depicted in the top panel along $\pi_r = 0$.

In both panels of Fig. 1, we do not see direct signs of a resonance. However, the rotation curve indicates where we have to look to find one. For example, to find the 1:3 resonance, one has to look between the first two initial conditions from the left of Fig. 1 or beyond the first initial condition from the right. Doing the latter provides a detail of the Poincaré section shown in the left panel of Fig. 2. The inset of this panel provides all the three expected
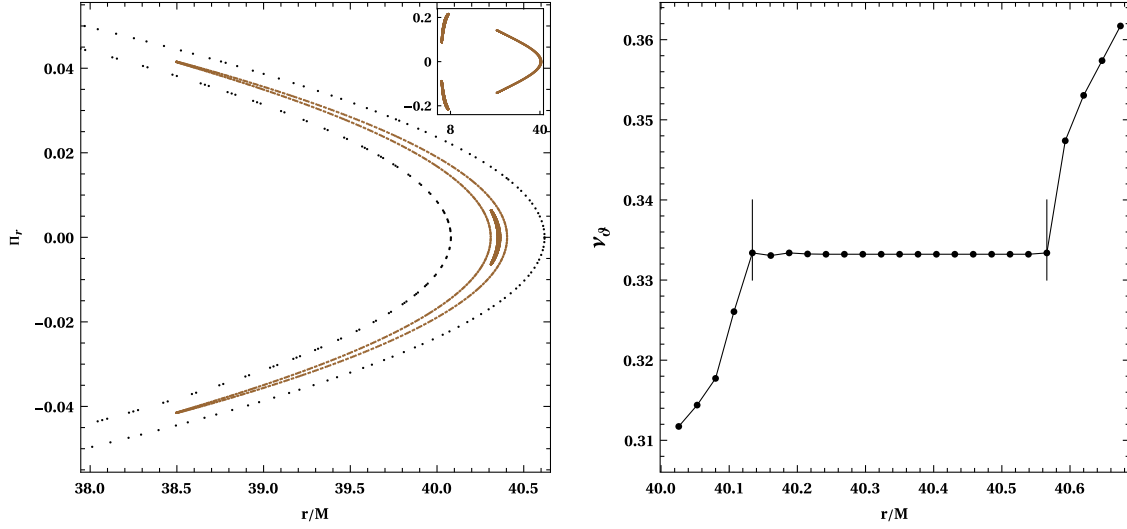
FIG. 2. The left panel shows a detail from the Poincaré section shown in Fig. 1 focusing on an island of stability of the 1:3 resonance, while the right panel shows the respective rotation curve with the characteristic plateau. The inset plot in the left panel represents the Poincaré section for a particular initial condition. For the radial distance, we choose from $40.026M$ to $40.674M$ with a step size of $0.027M$. Note that in the right curve for the rotation number, we have included all these data points. However, for the illustration of the resonance in the left panel, we have only shown a subset of the entire data set. This is only to make the plots more reader friendly. To indicate the resonance width w, we have drawn two lines parallel to ν_ϑ-axis at the endpoints of the plateau. The distance between these two endpoints along the r-axis corresponds to the width of the resonance w.

islands, while the main panel focuses just on one of the three islands of stability. The respective rotation curve is depicted in the right panel of Fig. 2, in which one can spot easily the characteristic plateau of the resonance. The length of this plateau measured along the radial coordinate r provides an adequately good measurement of the width of the resonance w.

B. Growth of resonance

As was already mentioned, resonances in dynamical systems can be approximated locally by the dynamics of a pendulum [46]. Using the above fact one can find that the square of the width of a resonance is proportional to the perturbation parameter [7,46,50]. By plotting the width of a resonance as a function of ϵ as we do in Fig. 3, we can correlate the perturbation parameter with ϵ. We investigate two main resonances (1:2 and 2:3) and the width of the resonances for each ϵ is determined by the length of each plateau on the corresponding rotation curve [7].

In Fig. 3 we fitted the data points for each resonance with the curve,

$$\log(w) = A + B\log(\epsilon). \qquad (30)$$

For the two under study 1:3 and 1:2 resonance, we found that $B = 0.997577$, and $B = 0.992058$, respectively. Given the slope in both cases is 1 (within a numerical error of 1%), we deduce that the perturbation parameter driving the

system away from integrability is proportional to ϵ^2. In other words, the system is integrable up to $\mathcal{O}(\epsilon)$.

This confirms our finding in Sec. II D, where we obtained that the Carter-like constant is valid up to $\mathcal{O}(\epsilon)$. It is interesting to note that in this feature the system is similar to the case of a spinning body moving in a Kerr black hole background. Namely, there is a Carter-like constant valid up to linear order in the spin of the secondary [51–55], while the perturbation parameter driving the system to nonintegrability appears to be proportional to the square of the spin [50].
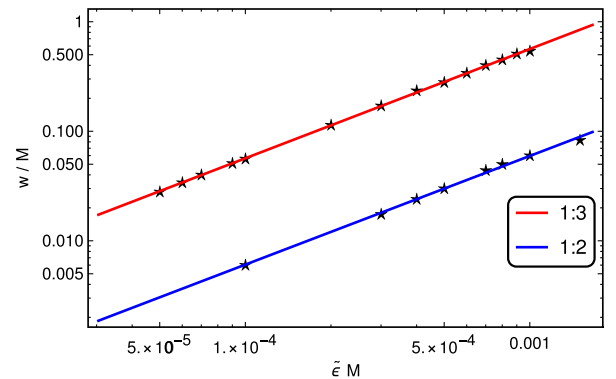

FIG. 3. The growth of the width of resonances as a function of the parameter ϵ in a log-log plot. The stars indicate the actual cases studied, while the lines are interpolations through these cases. To construct the above figures, we have used the following set of parameters: $\tilde{E} = 0.98$, $\tilde{L}_z = 3.8M$, and $a = 0.5M$.

IV. EFFECTS OF THE ELECTROMAGNETIC SELF-FORCE

The motion of accelerated charged body constitutes an interesting theoretical problem and has a long-standing history [56]. Starting with the seminal works of Lorentz, Abraham, and Poincaré in the Newtonian case [57], the contributions from Dirac [58], Landau [59], Dewitt, and Brehme for the relativistic domain have made remarkable expansion of the field [60]. Recent times have also witnessed a significant growth of interest in this topic [30,61]. For an excellent review we refer to [23]. In this section, we introduce the respective equations of motion in a ready to use format, and we discuss the resonant crossing effects for different initial conditions.

A. Equations of motion with the self-force

Before delving into the relativistic case, let us first discuss the Newtonian counterpart. In this limit, the equations of motion are given by Abraham-Lorentz equation [62]

$$m\frac{d\vec{\mathcal{V}}}{dt} = \vec{F}_{\text{ext}} + \frac{2q^2}{3}\frac{d^2\vec{\mathcal{V}}}{dt^2}, \qquad (31)$$

where $\vec{\mathcal{V}}$ is the velocity, $\vec{F}_{\text{ext}}$ is the external Lorentz force, and t is the time. Note that the second term on the right side captures the effect of the self-force of the moving charge, and it is provided by a derivative one order higher than the left side. This would lead to runaway solutions, which are physically inconsistent. One easy way to appreciate this is to switch off the external force, i.e., $F_{\text{ext}} = 0$, and we obtain $\mathcal{V} \sim \exp[3mt/(2q^2)]$. This diverges as t approaches infinity, and leads to a unphysical system. In order to avoid this pathology, one typically adopts the approach introduced by Landau and Lifshitz in [59], that is known as an "order-reduced" formalism. Within this approximation, the above expression can be written as

$$m\frac{d\vec{\mathcal{V}}}{dt} = \vec{F}_{\text{ext}} + \frac{2q^2}{3m}\frac{d\vec{F}_{\text{ext}}}{dt}. \qquad (32)$$

In the case of Lorentz force, we have

$$\vec{F}_{\text{ext}} = q(\vec{E}_{\text{ext}} + \vec{\mathcal{V}} \times \vec{B}_{\text{ext}}), \qquad (33)$$

where $\vec{E}_{\text{ext}}$ and $\vec{B}_{\text{ext}}$ are the electric and magnetic field respectively. If we assume that these fields are independent of time, we arrive at

$$\begin{aligned}\frac{d\vec{\mathcal{V}}}{dt} &= \vec{F}_{\text{ext}} + \frac{2q^3}{3m}\left(\frac{d\vec{\mathcal{V}}}{dt} \times \vec{B}_{\text{ext}}\right), \\ &= \vec{F}_{\text{ext}} + \frac{2q^3}{3m^2}(\vec{F}_{\text{ext}} \times \vec{B}_{\text{ext}}). \end{aligned} \qquad (34)$$

Once the external fields are known, we can obtain the final trajectory of the body. Therefore, this approach gives a self-consistent way to deal with the electromagnetic self-force of a charged body.

The relativistic correction to the Abraham-Lorentz equation was first introduced by Dirac and it is known as Abraham-Lorentz-Dirac equation [58]

$$m\frac{d\mathcal{U}^\mu}{d\tau} = F_{\text{ext}}^\mu + \frac{2q^2}{3}\left(\delta^\mu_\nu + \mathcal{U}^\mu\mathcal{U}_\nu\right)\frac{da^\nu}{d\tau}, \qquad (35)$$

where, F_{ext}^μ is the external Lorentz force, and given as $F_{\text{ext}}^\mu = qF^\mu{}_\nu\mathcal{U}^\nu$, and a^μ is the acceleration vector. By following the "order-reduced" approach discussed in the Newtonian case, we can write

$$a^\mu = (1/m)F_{\text{ext}}^\mu = \frac{q}{m}F^\mu{}_\nu\mathcal{U}^\nu. \qquad (36)$$

With the above substitution, we obtain

$$\begin{aligned}\frac{da^\mu}{d\tau} &= \frac{d^2\mathcal{U}^\mu}{d\tau^2} \\ &= \frac{q}{m}\left\{\left(\frac{dF^\mu{}_\nu}{d\tau}\right)\mathcal{U}^\nu + (q/m)F^\mu{}_\nu F^\nu{}_\alpha\mathcal{U}^\alpha\right\}, \\ &= \tilde{q}\frac{dF^\alpha{}_\beta}{dx^\mu}\mathcal{U}^\mu\mathcal{U}^\beta + \tilde{q}^2 F^\alpha{}_\beta F^\beta{}_\mu\mathcal{U}^\mu. \end{aligned} \qquad (37)$$

Finally, we can rewrite the above expression in a more reader friendly way as follows:

$$\begin{aligned}\frac{d\mathcal{U}^\mu}{d\tau} &= \tilde{q}F^\mu{}_\nu\mathcal{U}^\nu \\ &+ \frac{2q^2}{3m}(\delta^\mu_\nu + \mathcal{U}^\mu\mathcal{U}_\nu)\left(\tilde{q}\frac{dF^\nu{}_\beta}{dx^\gamma}\mathcal{U}^\gamma\mathcal{U}^\beta + \tilde{q}^2 F^\nu{}_\beta F^\beta{}_\gamma\mathcal{U}^\gamma\right). \end{aligned} \qquad (38)$$

For our future reference, we will call the prefactor of the second term in Eq. (35), i.e., $2q^2/3m$ as *radiation* parameter k, which actually scales the electromagnetic self-force felt by the charged body. In the case of EMRI driven by GSF, the analogous parameter would be the mass ratio $\eta = m/M$. In our system, the both parameters are formally related as follows:

$$\frac{k}{M} = \frac{2}{3}\tilde{q}^2\eta, \qquad (39)$$

Note that even if we fix the value of k (with respect to M), the mass ratio still depends on the arbitrary choice of specific charge. For instance, in our subsequent numerical examples we employ the value $k = 10^{-3}M$, for which $\eta \sim 10^{-1}(\tilde{q})^{-2}$. However, one has to keep in mind that the GSF and the electromagnetic self-force (ESF) are intrinsically different. Therefore, the mass ratio found from the

above formula is not directly relevant for GSF applied in EMRI systems.

In the curved spacetime, the self-forced motion of charged body is derived by DeWitt and Brehme [60],

$$\frac{D\mathcal{U}^\mu}{d\tau} = \tilde{q} F^\mu{}_\nu \mathcal{U}^\nu + f_R^\mu, \tag{40}$$

where f_R^μ is the radiation reaction given by the following expression:

$$f_R^\mu = k\left(\frac{D^2\mathcal{U}^\mu}{d\tau^2} + \mathcal{U}^\mu \mathcal{U}_\nu \frac{D^2\mathcal{U}^\nu}{d\tau^2}\right)$$
$$+ \frac{q^2}{3m}(R^{\mu\nu}\mathcal{U}^\nu + R^\nu_\lambda \mathcal{U}_\nu \mathcal{U}^\lambda \mathcal{U}^\mu) + 3k f_{\text{tail}}^{\mu\nu}\mathcal{U}_\nu, \tag{41}$$

with $f_{\text{tail}}^{\mu\nu}$ being the tail term

$$f_{\text{tail}}^{\mu\nu} = \int_{-\infty}^{\tau-0^+} D^{[\mu}G_{+\lambda'}^{\nu]}(z(\tau), z(\tau'))\mathcal{U}^{\lambda'} d\tau'. \tag{42}$$

The above expression contains an integral over the entire past of the body.

In the present case, we can simplify Eq. (40) further by considering the advantage of working in vacuum, and set the Ricci tensor to zero. Therefore, the second parenthesis in Eq. (41) vanishes and does not contribute. Moreover, by following the discussion in [30,61], we can also neglect the tail term, and finally arrive at

$$\frac{D\mathcal{U}^\mu}{d\tau} = \tilde{q} F^\mu{}_\nu \mathcal{U}^\nu + k\left(\frac{D^2\mathcal{U}^\mu}{d\tau^2} + \mathcal{U}^\mu \mathcal{U}_\nu \frac{D^2\mathcal{U}^\nu}{d\tau^2}\right). \tag{43}$$

We note that in its gravitational analog (i.e., in EMRI driven by GSF), the tail term (which corresponds to the effect of the backscattered gravitational radiation) remains relevant. Nevertheless, in the present electromagnetic model, its contribution is negligible as further discussed in Sec. VI, hence, we ignore this term in our calculations. This approximation is sufficient for our study as the key objective of our work is to study resonance crossing in a EMRI analog model with the help of a slow dissipation introduced by ESF.

Note that Eq. (43) matches with the flat spacetime relation given in Eq. (35), except for the fact that the ordinary derivative is now replaced with the covariant derivative. With this in mind, the expression for $D^2\mathcal{U}^\nu/d\tau^2$ can also be obtained directly from Eq. (37) by switching to covariant derivatives,

$$\frac{D^2\mathcal{U}^\mu}{d\tau^2} = \tilde{q}\frac{DF^\mu{}_\nu}{dx^\gamma}\mathcal{U}^\gamma \mathcal{U}^\nu + \tilde{q}^2 F^\mu{}_\nu F^\nu{}_\gamma \mathcal{U}^\gamma. \tag{44}$$

Unlike the Hamiltonian system discussed in Sec. II where the single parameter $\tilde{\epsilon}$ is sufficient to describe the

interaction with the EM field, here the situation becomes slightly more complicated and two independent parameters are needed. Namely, we have to deal with $\tilde{\epsilon}$ and k, when the radiation reaction is taken into account. Indeed, by inspecting Eqs. (43) and (44), we observe that although B_0 again couples with $\tilde{q}$ in both terms, the multiplication by the factor k is present only in the second term. Therefore, we need to set both values $\tilde{\epsilon}$ and k independently.

Moreover, by inserting (44) into (43), one notices that the leading perturbation parameter is ϵ, which comes from the Lorentz force Eq. (1) and the self-force introduces higher-order perturbations, i.e., $k\epsilon$ and $k\epsilon^2$. This indicates that even if the self-force is taken into account, the width of the resonance is mainly defined by ϵ.

In all the future references to ESF, we consider the equation of motion given by Eq. (43) and we parametrize the dissipating trajectories by $\tilde{\epsilon}$, k, and the initial values of $\tilde{E}$ and $\tilde{L}_z$.

B. Resonance crossings

From the Hamiltonian system, we are already informed about the existence of resonant islands for different initial conditions. We can place a body on an initial condition right outside a known resonance layer and dissipate the system using the self-force (43). The expectation is that the inspiralling body at a point will hit the resonance and cross it. Such a resonance crossing is shown in Fig. 4. Since the Hamiltonian system is nonintegrable, in accordance to the EMRI terminology we call these resonances prolonged [7,50].

The top panel of Fig. 4 shows a stroboscopic depiction of a $1\!:\!3$ resonance crossing on a Poincaré section,[1] which means that we used only every third point in the section's sequence. Using each point of this sequence as an initial condition we can evolve the system without the self-force in order to find the rotation number for each of these points as was also done in [7]. The result is a rotation curve shown in the bottom panel of Fig. 4, where the rotation numbers are plotted with the respect to the proper time. The plateau at $1\!:\!3$ indicates the points corresponding to the crossing of the resonance.

With the dissipation turned on, previously constant quantities will be evolving. Figure 5 shows a typical evolution of the energy $\tilde{E}$, the angular momentum $\tilde{L}_z$, the relative error of the Hamiltonian $\Delta\tilde{H}/\tilde{H}$ and $\tilde{\mathcal{K}}$.[2] The energy and the angular momentum follow an almost linear decline, while the Hamiltonian is conserved up to numerical precision. The behavior of the quantity $\tilde{\mathcal{K}}$ deserves more attention. Unlike the other three quantities, it is actually not an integral of motion and its value oscillates even without

---

[1]Note that since the system is dissipating the use of the term Poincaré section is approximative, i.e., a loan from the Hamiltonian nondissipative case.

[2]Recall that $\tilde{\mathcal{K}}$ is actually not a constant when the system is nonlinear in ϵ.
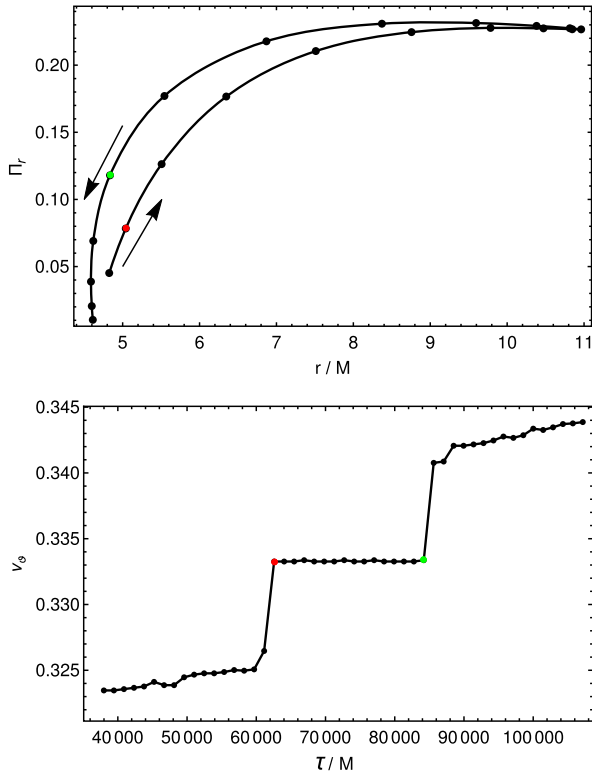
FIG. 4. The plots show a case of a resonance crossing in the dissipative system with an attractive Lorentz force. The trajectory of the inspiral starts with $\tilde{E} = 0.98$, $\tilde{L}_z = 3.3M$, $\pi_r = 0$, $\theta = \pi/2$, initial value of the radial coordinate is chosen to be $r = 40.0995M$, and the rest parameters of the system are $\tilde{\epsilon} = -10^{-3}M^{-1}$, and $k = 10^{-3}M$. The top panel shows a stroboscopic depiction of the Poincaré section, with the red dot indicating the entrance of the inspiral into the resonance and the green the exit. The arrows indicate the way the stroboscopic depiction evolves on the section. The bottom panel shows the rotation curve, i.e., the rotation number as a function of the proper time. The 1:3 resonance is indicated by the presence of the characteristic plateau on the rotation curve.

the self-force. Moreover, if the self-force is introduced, $\tilde{\mathcal{K}}$ exhibits an abrupt drop during the resonance crossing. Such jumps are quite common at resonance crossings induced by GSF [16,20] and they typically scale as the square root of the parameter which perturbs the system and induces dissipation (i.e., the square root of the mass ratio in the case of GSF). In our model, the perturbation parameter $\tilde{\epsilon}$ is independent of the self-force effects captured by the parameter k. As was already discussed in Sec. IV, the width of the resonance should be determined mainly by $\tilde{\epsilon}$. A reasonable expectation is that the jump in $\tilde{\mathcal{K}}$ should be proportional to the width of the resonance. To confirm this, we did some numerical checks. For resonance 1:2, with $\tilde{\epsilon} = 10^{-3}M^{-1}$, and $r_i = 41.2M$, the jump in $\tilde{\mathcal{K}}$ (the change in its value between entering and leaving the resonance) is $\sim 0.08M^2$ which is approximately $\sim \sqrt{\tilde{\epsilon}M}$. For resonance 1:3, the jump in $\tilde{\mathcal{K}}$ for $r_i = 40.098M$ and $\tilde{\epsilon} = 10^{-3}M^{-1}$ is

$\sim 0.6M^2$, i.e., an order of magnitude higher than $\sqrt{\tilde{\epsilon}M}$. We speculate that this discrepancy is caused by different coefficients entering the proportional relation between the width and the jump. However, this demands a meticulous investigation, which we plan for a future work.

V. COMPARISON BETWEEN THE ADIABATIC APPROXIMATION AND FULL SELF-FORCE

One of the key objectives of this paper is to compare the adiabatic approximation with the instantaneous electromagnetic self-force computations. This may hint us to shape our ideas in the GSF sector as well. As the application of self-force is relatively easier in the electromagnetic case than its gravitational counterpart, we can exploit this advantage. For the adiabatic approximation, we have not followed the traditional approach to obtain the fluxes due to energy and angular momentum, as typically done in literature [13]. Namely, in the traditional adiabatic approach of an EMRI the evolution of the system tracks the slow dissipation of the constants of motion; energy, momentum and Carter constant. Since the geodesic motion in a Kerr background is integrable, one can correlate the values of the constants with the orbital parameters of the body and track the inspiral. In our case, however, the system (unless being linearized in ϵ) is nonintegrable and lacking the Carter-like constant. To employ an adiabatic scheme for the nonintegrable system and compare it with the full self-force results we do the following. We use the energy and angular momentum values obtained from the instantaneous self-force to fit the respective data sets, and obtain the energy and momentum as functions of time. In other words, we can write energy and momentum as follows:

$$E(\tau) = E(0) + \sum_{n=1}^{N} a_n \tau^n,$$

$$L_z(\tau) = L_z(0) + \sum_{n=1}^{N} b_n \tau^n, \qquad (45)$$

where a_n and b_n are usual expansion coefficients capturing the effects of the self-force, and $E(0)$ and $L_z(0)$ are the initial values of energy and momentum, respectively. The instantaneous self-force comes with the advantage of adding as many order of correction as we want, and it is only a matter of higher-order fitting, i.e., higher N. In an example discussed in the Appendix, we indicate that the order of fitting may affect the final outcome of the resonance crossing. Our numerical investigation showed that the mismatch is marginal if we consider $N \geq 2$. In most cases when reproducing the plots, we consider the fitting to be a fourth-order polynomial ($N = 4$).

Our adiabatic scheme is similar with those used in [4,6,7,63], the only difference is that those studies used
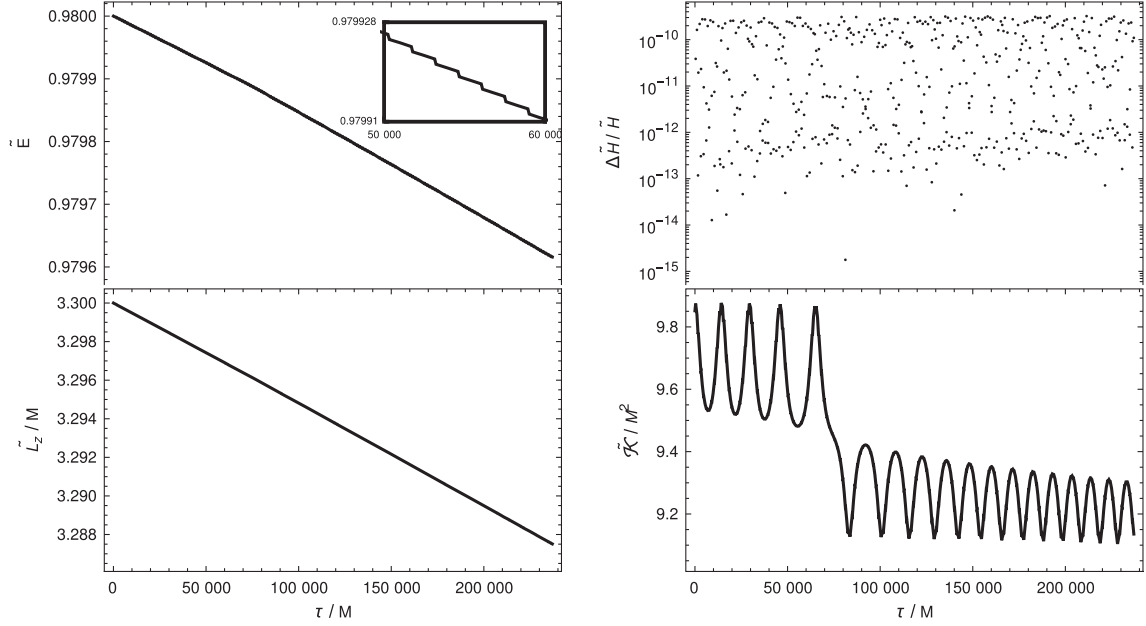
FIG. 5. Dissipation for various adiabatically changing quantities are shown: the initial values of different parameters are $r_i = 40.09950M$, $\tilde{E} = 0.98$, and $\tilde{L}_z = 3.3M$. The top left shows the dissipation of the energy with the inset focusing on a small part of the graph so that the oscillations become visible; the bottom left shows how the angular momentum is dissipating over time; the top right panel shows that the variation of the relative error $\Delta\tilde{H}/\tilde{H}$ is $\sim \mathcal{O}(10^{-15})$ to $\mathcal{O}(10^{-10})$. The bottom right depicts the evolution of $\tilde{\mathcal{K}}$, as given in Eq. (15). This evolution differs significantly from the other quantities and it is easy to spot the jump which corresponds to the resonance.

averaged fluxes instead of using the instantaneous self-force. As in these studies the absence of a Carter-like constant limits our dissipation scheme in using just the energy and the angular momentum losses. By using the fitted function of the energy and momentum as pointed out in Eq. (45), we obtain P^t and P^ϕ as a function of time,

$$P^t = E(\tau) + \frac{2Mr[E(\tau)(r^2 + a^2) - aL_z(\tau)]}{\Delta\Sigma} - a\epsilon,$$

$$P^\phi = \frac{L_z(\tau)\csc^2\theta}{r^2 + a^2} + \frac{2aMr[E(\tau)(r^2 + a^2) - aL_z(\tau)]}{(r^2 + a^2)\Delta\Sigma} - \epsilon/2.$$

(46)

The self-force corrections are encoded within the time evolution of energy and angular momentum. To obtain the other components namely P^r and P^θ, we use Eq. (1), which does not include the dissipative effects. The entire premise of using the adiabatic approximation here is to averaged out the instantaneous self-force contribution and ignore some of its components. By comparing the results obtained from the adiabatic evolution with the self-force one, we intend to deduce arguments relevant for the EMRI gravitational counterpart.

In Fig. 6, we consider a typical example where the adiabatic evolution is shown. The detailed parameter space and the fitting parameters are given in the caption of the plot. If we ignore the scattered points, we can see that the relative error in the Hamiltonian steadily grows (top panel
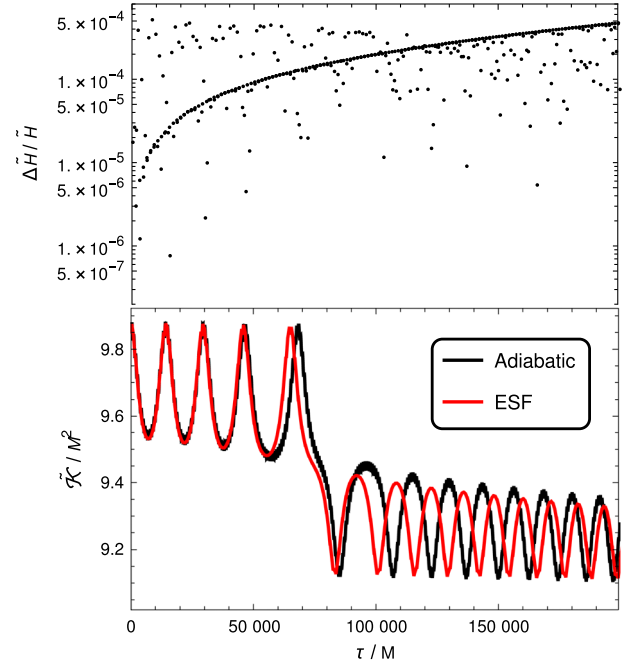

FIG. 6. The change in the relative error of the Hamiltonian (top panel) and of the $\tilde{\mathcal{K}}$ quantity (bottom panel) as the binary evolves within the adiabatic approximation. The initial conditions are similar to what being used in Fig. 5. We use a fourth order polynomial fit for the energy and momentum, and the fitting parameters for the energy and momentum are $a_1 = -1.42 \times 10^{-9}$, $a_2 = -1.37 \times 10^{-15}$, $a_3 = 2.17 \times 10^{-21}$, $b_1 = -5.1 \times 10^{-8}$, $b_2 = -1.06 \times 10^{-14}$, and $b_3 = 1.38 \times 10^{-20}$.

of Fig. 6) in contrast to the self-force calculation (right top panel of Fig. 5). The latter shows that the Hamiltonian remains conserved up to $\mathcal{O}(10^{-10})$, which implies a numerical precision accuracy. Hence, one of the side-effects of using our scheme for adiabatic approximation is that the mass of the inspiralling body changes with time.

The evolution of $\tilde{\mathcal{K}}$ is also affected by the adiabatic approximation as can be seen form the bottom plot of Fig. 6, where it is compared with the instantaneous electromagnetic self-force calculations. In particular, the difference grows in time, and becomes more prominent near the resonance. This might be an artifact of the employed adiabatic approximation, which could be enhanced by the fact that we ignored the evolution of $\tilde{\mathcal{K}}$. It has been shown by Isoyama *et al.* [64,65], and recently by Nasipak and Evans [66], that the evolution of the Carter constant is crucial in order to describe the adiabatic evolution of EMRIs through resonances. Therefore, it could be interesting to include it in the case of electromagnetic case as well, but, we leave this for a future work.

The above discussed discrepancies have as a result that the evolution from the same initial conditions are not giving the same time Δt_r that the inspiral spends in the resonance for the adiabatic and the self-force approach (Fig. 7). In order to obtain Δt_r for different initial conditions, we follow the prescription shown in Ref. [7]. Given an initial condition, we evolve the dissipative system for a sufficiently long time to obtain $\sim 10^3$ to 10^4 points on a Poincaré section. By referring to Fig. 4, we encounter similar structure in the Poincaré section which hints where and when the particle meets the resonance. Once we pin down the locations of the resonance, we note the coordinates of these points, along with the corresponding four-momentum, energy, angular momentum and the value of the Hamiltonian. Afterwards, we evolve each of these points without the ESF for a significant amount of time and evaluate the rotation number. We repeat this procedure

for each initial condition given in Fig. 7. By looking at the values of Δt_r shown in Fig. 7 it appears that the time spent by the inspiral in the resonance to be qualitatively the same for both approaches. Even exotic cases, like those that the inspiral enters a resonance, but does not leave, seems to be reproduced both by a self-force and an adiabatic evolution. Note that this exotic effect is similar with the sustained resonances [67] appearing in EMRI studies [68]. Hence, the adiabatic scheme appears to be sufficiently faithful to the instantaneous self-force evolution.

In Fig. 7 the initial conditions giving the "sustained" type of resonance crossings are indicated by two nearby vertical lines. These lines lie between a maximum and a minimum of the $\Delta t_r(r)$ plot. The absence of these lines in the self-force evolution scheme through the 1:3 resonance (left plot of Fig. 7) is probably caused by its very small width. The minima of the $\Delta t_r(r)$ plot correspond to inspirals crossing through the vicinity of the unstable periodic orbit of the resonance. The maxima of the $\Delta t_r(r)$ plot correspond to inspirals entering sufficiently deep into the islands of stability (formed around the stable periodic orbit), which spend a considerable time period within the island before they exit the resonance. On the other hand, if an inspiral enters too deep into the island of stability, it becomes trapped by the resonance for a very long time which exceeds the integration time.

VI. ASTROPHYSICAL RELEVANCE OF THE PARAMETERS

The model was discussed in geometrized units scaled by the rest mass of the central black hole. In order to check the astrophysical consistency of the employed values we employ the relation between radiation parameter k, mass ratio η, and specific charge $\tilde{q}$ given by Eq. (39). In particular, for our numerical examples we employ the value $k = 10^{-3}M$, for which the mass ratio yields
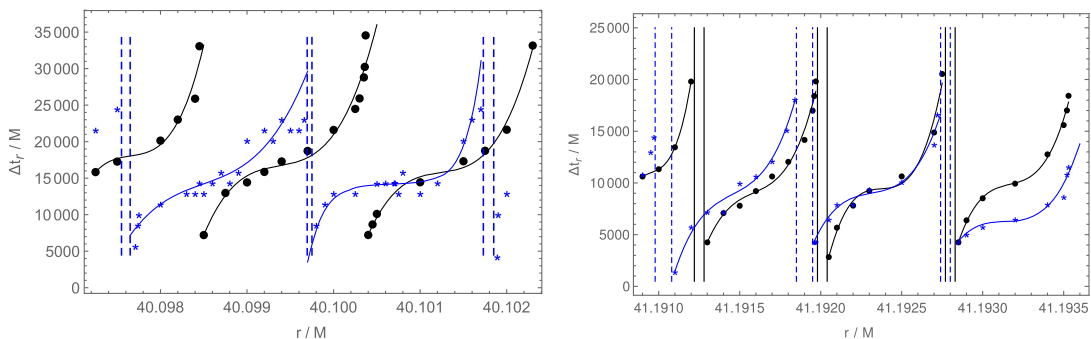

FIG. 7. Periods of time Δt_r spent by a body within the resonance (as a function of the initial radius) comparing the full self-force description (black) with the approximated adiabatic evolution (blue). The space between two nearby vertical dashed blue lines indicates the initial radii for which the body following the adiabatic evolution enters the resonance and we do not see it leaving it. In the right plot the space between two nearby vertical continuous black lines indicate the same thing for the self-force driven evolution. The left plot shows the 1:3 resonance, while the right the 1:2. The following values for the parameters were used: $\tilde{E}(0) = 0.98$, $\tilde{L}_z(0) = 3.8M$, $a = 0.5M$, $\tilde{e} = -10^{-3}M^{-1}$, and $k = 10^{-3}M$.

$\eta \sim 10^{-1}(\tilde{q})^{-2}$. Fixing the mass ratio at the value relevant for EMRI systems as $\eta = 10^{-4}$ thus leads to $\tilde{q} \sim 1$. Generally, the upper limit on the relevant value of the specific charge would be set by an electron with $|\tilde{q}_e| \sim 10^{21}$ in geometrized units. On the other hand, the theoretical limit on the charge of the static (Reissner-Nordström) black hole is $|\tilde{q}_{RN}| = 1$. For the value employed in our analysis, $|\tilde{\epsilon}| = |\tilde{q}B_0| = 10^{-3}M^{-1}$, we may then retrieve the value of magnetic induction in physical units if M is specified,

$$(B)_{SI} = \frac{\tilde{\epsilon}}{\tilde{q}} \frac{c}{1472} \left(\frac{M_\odot}{M}\right) \sqrt{\frac{k_C}{G}}. \qquad (47)$$

In particular, for a black hole in the center of M87 galaxy with mass $M \sim 10^{10} M_\odot$ [69] we obtain $(B)_{SI} \sim 10^2 T$. This is several orders of magnitude more than the value derived from the recent observations of M87 with the Event Horizon Telescope [70]; however, still within the range of realistic estimates for accreting black holes [71,72].

Dissipative trajectories studied in the present paper were evolved by Eq. (43) in which the contribution of the tail term was neglected. While the estimates presented in [61] justify such approximation for the case of a single charged particle such as electron near a magnetized black hole, we need to verify its validity for our scenario of an EMRI analog. To proceed, we employ results from [73], where the self-force on the static point charge q of mass m near a (Schwarzschild) black hole of mass M is computed. In such system with no external electromagnetic field, the self-force appears solely due to the interaction between the field of the point charge and the black hole curvature and thus allows us to estimate the contribution of the tail term (the only part of the self-force which remains when the magnetic field is switched off in our model). The ratio Ψ between the self-force and the gravitational force (which remains dominant in our case as we set $|\epsilon| = 10^{-3}$), is shown [73] to have its maximum close to horizon (namely at $r = 3M$ in Schwarzschild spacetime) and drops as $\Psi \propto 1/r$ farther from the black hole. In particular, the maximum value Ψ^{max} (expressed by quantities in SI units) is given as

$$\Psi^{\mathrm{max}} = \frac{k_C}{3\sqrt{3}G} \left(\frac{q^2}{mM}\right)_{SI} = \frac{k_C(\tilde{q})^2_{SI}\eta}{3\sqrt{3}G}, \qquad (48)$$

where k_C and G are he Coulomb and the gravitational constants, respectively.

For an electron and a black hole of one stellar mass we get $\Psi^{\mathrm{max}} \sim 10^{-19}$. For the most unfavourable EMRI case of $\eta = 10^{-4}$ and $\tilde{q} = 1$ (extremal Reissner-Nordström black hole) the ratio yields $\Psi^{\mathrm{max}} \sim 10^{-5}$ which makes this contribution negligible even in this worst-case scenario, while for radii corresponding to our numerical examples this ratio reduces at least to $\Psi^{\mathrm{max}} \sim 10^{-6}$.

The above analysis shows that our model and employed approximations are generally consistent with the conditions encountered in astrophysical systems. However, we stress that it is not proposed as a model directly corresponding to an EMRI and, in particular, the values of mass ratio formally expressed in Eq. (39) cannot be straightforwardly identified with the mass ratio parameter in EMRI system driven by GSF. Instead of modeling particular dynamic properties of an EMRI, the motivation of our analog model is more general and our aim is to study fundamental properties of resonances affected by a nonintegrable perturbation and the behavior of trajectories crossing such resonances due to dissipation caused by a self-force. Our setup allows us to test the reliability of the adiabatic approximation. In particular, in the present work we raised (and positively answered) the question whether the evolution of resonance-crossing trajectories might be reasonably approximated by the adiabatic (averaged) prescription for the dissipation of $\tilde{E}$ and $\tilde{L}_z$.

VII. SUMMARY AND DISCUSSION

In this work we studied the dynamics of a charged body orbiting a magnetized Kerr black hole. This nonintegrable system bears some dynamical similarities with the system of a spinning body moving in the pure Kerr background. In particular, the trajectories in both systems deviate from the geodesics; in the first system, this is due to Lorentz force, while in the second due to spin-curvature coupling. In both systems, the induced perturbation breaks the full integrability. In the first case, it is the presence of the magnetic field, while in the second, it is the spin of the secondary body, which makes the system nonintegrable. In both systems there is a Carter-like constant, which holds up to linear order in the perturbation term and effects of nonintegrability appear due to terms quadratic in the perturbation. This fact has recently been demonstrated for the spinning body [50,55], while for the charged body orbiting a magnetized Kerr black hole we showed that in Sec. II of the present paper. The above reasons make the latter system an interesting *electromagnetic analog* of an EMRI, which allows to study the dynamics of the inspiralling body during the resonance crossing induced by the self-force.

In our study we induced dissipation to the charged body using two approaches. First, we considered the instantaneous electromagnetic self-force without its tail terms. We evolved the system through a 1∶3 and 1∶2 resonances and studied the crossings of these resonances for various initial conditions. During the evolution of these crossings, we computed losses of the energy, the angular momentum along z and the Carter-like quantity $\tilde{K}$. We noticed that although the energy and the angular momentum were changing relatively smoothly, $\tilde{K}$ experienced an abrupt change due to resonance crossing. It is not clear why only

$\tilde{\mathcal{K}}$ (and not the other constants) exhibits such behavior. Is it a feature of the electromagnetic self-force, which will not be reproduced in the GSF case? Further investigation is needed to determine the reason of this discrepancy.

Since we calculated how the energy and angular momentum change along each trajectory, we were able to interpolate the time evolution of these quantities. Using these interpolations, we applied an adiabatic scheme to evolve orbits crossing 1:3 and 1:2 resonances. This allowed us to test whether the adiabatic scheme represents a faithful approximation of an instantaneous self-force. We were able to check that the adiabatic crossings of the resonance last for time intervals that are quantitatively comparable with those given by the instantaneous self-force. This does not mean that there are not discrepancies, like the presence of "sustained" resonances in the case of the 1:3 resonance, which occur in the adiabatic approximation, but not with the full self-force. However, this discrepancy might be an artifact of our adiabatic scheme in which the dissipation of the Carter-like constant is not prescribed. We plan to further investigate this issue and possibly optimize our adiabatic approximation.

Nevertheless, the fact that we got faithful results regarding the resonance crossing duration without prescribing the dissipation of the Carter-like constant is remarkable and might also have an application in nonintegrable systems where a Carter-like constant does not exist even to a linear order with respect to the perturbation. Our results strongly indicate that it is sufficient to adiabatically dissipate the system just through the energy and angular momentum, in order to find the correct times that resonance crossings last in EMRIs.

Since we studied an analog model driven by an electromagnetic self-force, any particular numerical values of the observable quantities (e.g., time intervals spent in resonances) are not directly relevant from the observational perspective of EMRIs. However, the main result of our analysis, which is the remarkable correspondence between the instantaneous self-force and its adiabatic approximation, is supposed to hold for a significantly broader class of nonintegrable dynamical systems with dissipation. In particular, our results provide an indication that adiabatic approximation might be sufficient to faithfully model intricate dynamics of resonance crossing of an EMRI.

ACKNOWLEDGMENTS

APPENDIX: ADIABATIC APPROXIMATION

Let us now point out a few artifacts of the adiabatic approximation employed in our work. We found that close

to the change from the maxima to the minima in Fig. 7 the adiabatic framework begins to encounter a problematic behavior.

We demonstrate in Fig. 8 how the polynomial fit of energy and angular momentum may affect the adiabatic evolution. Figure 8 shows the radial coordinate of every third crossing of the inspiral through the equatorial plane when $\pi^\theta > 0$ as a function of the proper time τ. Basically, we use a stroboscopic depiction of a Poincaré section as was discussed when introducing the top panel of Fig. 4. The orbit starts on the equatorial plane with $\pi^r = 0$ and $r = 40.09966M$, but we use for aesthetic reasons the immediately next crossing through the Poincaré section to produce the stroboscopic picture in both the top panel of Fig. 4 and in Fig. 8. In the latter figure high peaks correspond to the part of the inspiral moving on KAMs away from the resonance, while low peaks correspond to the phase of the evolution spend in the resonance on an island of stability (see top panel Fig. 4). To reproduce the top panel of Fig. 8, we use a second-order polynomial fit for the energy and the angular momentum. The multiple low peaks indicate that the inspiral spend a significant number of cycles in the resonance. However, this feature simply disappears if we consider a higher order polynomial fit, as depicted in the lower panel of Fig. 8. Hence, as we move closer and closer to the jump from maxima to minima, we
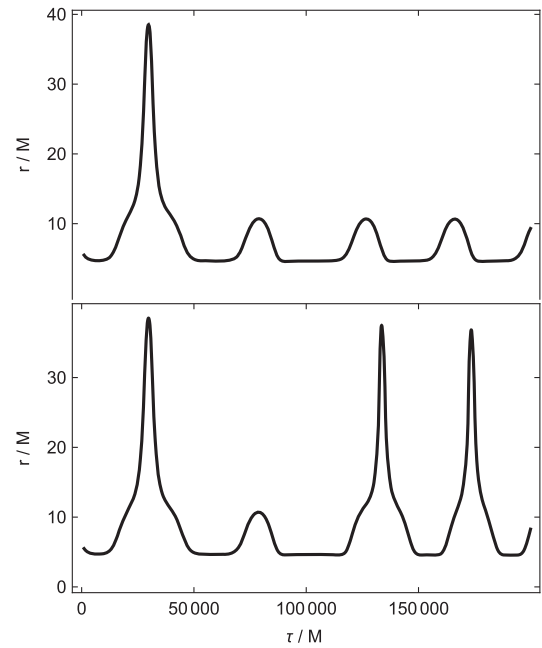

FIG. 8. This figure shows how higher-order terms in the fitted energy and angular momentum affect the resonance crossing. For the upper panel, we set $E(\tau) = E_0 + a_1\tau + a_2\tau^2$, while for the lower pane, we set $E(\tau) = E_0 + a_1\tau + a_2\tau^2 + a_3\tau^3$. The upper case, the body seems to repeat the loop several times, while for the lower case, the body only cross it once. This example is for the initial distance $r = 40.09966M$, $\tilde{E}(0) = 0.98$, $\tilde{L}_z(0) = 3.8M$, $a = 0.5M$, $\epsilon = -10^{-3}$, and $k = 10^{-3}$.

need higher-order polynomial fit to avoid such artifacts. Nonetheless, for some initial conditions, as shown within the dashed blue lines of Fig. 7, it is not possible to avoid inspirals being trapped in the resonance. This kind of entrapment seems to be a feature of the system, since we can see it happening also in the self-force driven evolution.

For the second example, we again consider the adiabatic approximation close to the jump from maxima to minima. In Fig. 9, we provide an example of the adiabatic evolution such that it crosses a 1:2 resonance. We notice that the journey through the resonance is not smooth, and some points deviate from this plateau. This is not an numerical artifact and not present for the full self-force computations. However, we observe this feature for both 1:2 and 1:3 resonances when evolving the system adiabatically.
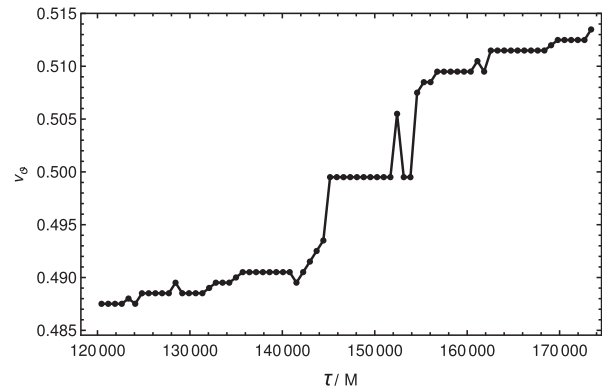

FIG. 9. The rotation curve for a dissipative system as it inspirals through 1:2 resonance. The initial conditions are $\tilde{E}(0) = 0.98$, $\tilde{L}_z(0) = 3.8M$, $a = 0.5M$, $\epsilon = -10^{-3}$, $k = 10^3$, $r = 41.19205M$, and $\theta = \pi/2$.

[1] A. Lichtenberg and M. Lieberman, *Regular and Chaotic Dynamics* (Springer, New York, NY, 1992).

[2] V. I. Arnold, Proof of a theorem of A. N. KOLMOGOROV on the invariance of quasi-periodic motions under small perturbations of the Hamiltonian, Russ. Math. Surv. **18**, 9 (1963).

[3] T. A. Apostolatos, G. Lukes-Gerakopoulos, and G. Contopoulos, How to Observe a Non-Kerr Spacetime Using Gravitational Waves, Phys. Rev. Lett. **103**, 111101 (2009).

[4] G. Lukes-Gerakopoulos, T. A. Apostolatos, and G. Contopoulos, Observable signature of a background deviating from the Kerr metric, Phys. Rev. D **81**, 124005 (2010).

[5] K. Destounis, A. G. Suvorov, and K. D. Kokkotas, Testing spacetime symmetry through gravitational waves from extreme-mass-ratio inspirals, Phys. Rev. D **102**, 064041 (2020).

[6] K. Destounis, A. G. Suvorov, and K. D. Kokkotas, Gravitational Wave Glitches in Chaotic Extreme-Mass-Ratio Inspirals, Phys. Rev. Lett. **126**, 141102 (2021).

[7] G. Lukes-Gerakopoulos and V. Witzany, Nonlinear effects in EMRI dynamics and their imprints on gravitational waves, in *Handbook of Gravitational Wave Astronomy* (Springer, Singapore, 2021), p. 42, 10.1007/978-981-15-4702-7_42-1.

[8] D. Bronicki, A. Cárdenas-Avendaño, and L. C. Stein, Tidally-induced nonlinear resonances in EMRIs with an analogue model, arXiv:2203.08841.

[9] S. Babak, J. Gair, A. Sesana, E. Barausse, C. F. Sopuerta, C. P. L. Berry, E. Berti, P. Amaro-Seoane, A. Petiteau, and A. Klein, Science with the space-based interferometer LISA. V. Extreme mass-ratio inspirals, Phys. Rev. D **95**, 103012 (2017).

[10] L. Barack and A. Pound, Self-force and radiation reaction in general relativity, Rep. Prog. Phys. **82**, 016904 (2019).

[11] A. Pound and B. Wardell, Black hole perturbation theory and gravitational self-force, arXiv:2101.04592.

[12] M. van de Meent, Gravitational self-force on generic bound geodesics in Kerr spacetime, Phys. Rev. D **97**, 104033 (2018).

[13] S. Drasco and S. A. Hughes, Gravitational wave snapshots of generic extreme mass ratio inspirals, Phys. Rev. D **73**, 024027 (2006).

[14] S. Isoyama, R. Fujita, A. J. K. Chua, H. Nakano, A. Pound, and N. Sago, Adiabatic Waveforms from Extreme-Mass-Ratio Inspirals: An Analytical Approach, Phys. Rev. Lett. **128**, 231101 (2022).

[15] M. L. Katz, A. J. K. Chua, L. Speri, N. Warburton, and S. A. Hughes, Fast extreme-mass-ratio-inspiral waveforms: New tools for millihertz gravitational-wave data analysis, Phys. Rev. D **104**, 064047 (2021).

[16] É. É. Flanagan and T. Hinderer, Transient Resonances in the Inspirals of Point Particles into Black Holes, Phys. Rev. Lett. **109**, 071102 (2012).

[17] J. Brink, M. Geyer, and T. Hinderer, Orbital Resonances Around Black Holes, Phys. Rev. Lett. **114**, 081102 (2015).

[18] J. Brink, M. Geyer, and T. Hinderer, Astrophysics of resonant orbits in the Kerr metric, Phys. Rev. D **91**, 083001 (2015).

[19] S. Mukherjee and S. Tripathy, Resonant orbits for a spinning particle in Kerr spacetime, Phys. Rev. D **101**, 124047 (2020).

[20] C. P. L. Berry, R. H. Cole, P. Cañizares, and J. R. Gair, Importance of transient resonances in extreme-mass-ratio inspirals, Phys. Rev. D **94**, 124042 (2016).

[21] A. Sarkar, A. Ali, and S. Nasri, Perturbative correction terms to electromagnetic self-force due to metric perturbation: Astrophysical and cosmological implications, Eur. Phys. J. C **81**, 725 (2021).

[22] P. Zimmerman and E. Poisson, Gravitational self-force in nonvacuum spacetimes, Phys. Rev. D **90,** 084030 (2014).

[23] E. Poisson, The motion of point particles in curved spacetime, Living Rev. Relativity **7,** 6 (2004).

[24] A. Pound, E. Poisson, and B. G. Nickel, Limitations of the adiabatic approximation to the gravitational self-force, Phys. Rev. D **72,** 124001 (2005).

[25] A. Pound and E. Poisson, Multiscale analysis of the electromagnetic self-force in a weak gravitational field, Phys. Rev. D **77,** 044012 (2008).

[26] R. M. Wald, Black hole in a uniform magnetic field, Phys. Rev. D **10,** 1680 (1974).

[27] J. Bicak and V. Janis, Magnetic fluxes across black holes, Mon. Not. R. Astron. Soc. **212,** 899 (1985).

[28] V. Karas, O. Kopáček, and D. Kunneriath, Magnetic neutral points and electric lines of force in strong gravity of a rotating black hole, Int. J. Astron. Astrophys. **3,** 18 (2013).

[29] S. A. Balbus and J. F. Hawley, Instability, turbulence, and enhanced transport in accretion disks, Rev. Mod. Phys. **70,** 1 (1998).

[30] M. Kološ, A. Tursunov, and Z. Stuchlík, Radiative Penrose process: Energy gain by a single radiating charged particle in the ergosphere of rotating black hole, Phys. Rev. D **103,** 024021 (2021).

[31] J. Kovář, O. Kopáček, V. Karas, and Z. Stuchlík, Off-equatorial orbits in strong gravitational fields near compact objects—II: halo motion around magnetic compact stars and magnetized black holes, Classical Quantum Gravity **27,** 135006 (2010).

[32] O. Kopáček, V. Karas, J. Kovář, and Z. Stuchlík, Transition from regular to chaotic circulation in magnetized coronae near compact objects, Astrophys. J. **722,** 1240 (2010).

[33] A. M. Al Zahrani, Escape of charged particles moving around a weakly magnetized Kerr black hole, Phys. Rev. D **90,** 044012 (2014).

[34] O. Kopáček and V. Karas, Near-horizon structure of escape zones of electrically charged particles around weakly magnetized rotating black hole, Astrophys. J. **853,** 53 (2018).

[35] O. Kopáček and V. Karas, Near-horizon structure of escape zones of electrically charged particles around weakly magnetized rotating black hole. II. Acceleration and escape in the oblique magnetosphere, Astrophys. J. **900,** 119 (2020).

[36] C. W. Misner, K. S. Thorne, and J. A. Wheeler, *Gravitation* (Princeton University Press, Princeton, NJ, 2017).

[37] V. S. Beskin, A. Balogh, M. Falanga, and R. A. Treumann, Magnetic fields at largest universal strengths: Overview, Space Sci. Rev. **191,** 1 (2015).

[38] J. Bičák and T. Ledvinka, Electromagnetic fields around black holes and Meissner effect, Nuovo Cimento B Ser. **115,** 739 (2000), arXiv:gr-qc/0012006.

[39] N. Gürlebeck and M. Scholtz, Meissner effect for weakly isolated horizons, Phys. Rev. D **95,** 064010 (2017).

[40] N. Gürlebeck and M. Scholtz, Meissner effect for axially symmetric charged black holes, Phys. Rev. D **97,** 084042 (2018).

[41] O. Kopáček, T. Tahamtan, and V. Karas, Null points in the magnetosphere of a plunging neutron star, Phys. Rev. D **98,** 084055 (2018).

[42] V. Karas, O. Kopáček, and D. Kunneriath, Influence of frame-dragging on magnetic null points near rotating black holes, Classical Quantum Gravity **29,** 035010 (2012).

[43] B. Carter, Global structure of the Kerr family of gravitational fields, Phys. Rev. **174,** 1559 (1968).

[44] B. Carter, Black hole equilibrium states, in *Black Holes*, edited by C. deWitt and B. deWitt (Gordon and Breach Science Publishers, New York, 1973).

[45] S. Mukherjee and K. Rajesh Nayak, Carter constant and angular momentum, Int. J. Mod. Phys. D **27,** 1750180 (2018).

[46] A. Morbidelli, *Modern Celestial Mechanics: Aspects of Solar System Dynamics*, 1st ed. (Taylor & Francis, London, 2002).

[47] G. D. Birkhoff, Proof of Poincaré's geometric theorem, Trans. Am. Math. Soc. **14,** 14 (1913).

[48] N. Voglis and C. Efthymiopoulos, Angular dynamical spectra. A new method for determining frequencies, weak chaos and cantori, J. Phys. A **31,** 2913 (1998).

[49] G. Contopoulos, *Order and Chaos in Dynamical Astronomy* (Springer Science & Business Media, New York, 2002).

[50] O. Zelenka, G. Lukes-Gerakopoulos, V. Witzany, and O. Kopáček, Growth of resonances and chaos for a spinning test particle in the Schwarzschild background, Phys. Rev. D **101,** 024037 (2020).

[51] R. Rüdiger, Conserved quantities of spinning test particles in general relativity. I, Proc. R. Soc. A **375,** 185 (1981).

[52] R. Rüdiger, Conserved quantities of spinning test particles in general relativity. II, Proc. R. Soc. A **385,** 229 (1983).

[53] G. Gibbons, R. H. Rietdijk, and J. Van Holten, SUSY in the sky, Nucl. Phys. **B404,** 42 (1993).

[54] T. Tanaka, Y. Mino, M. Sasaki, and M. Shibata, Gravitational waves from a spinning particle in circular orbits around a rotating black hole, Phys. Rev. D **54,** 3762 (1996).

[55] V. Witzany, Hamilton-Jacobi equation for spinning particles near black holes, Phys. Rev. D **100,** 104030 (2019).

[56] F. Rohrlich, *Classical Charged Particles: Foundations of Their Theory* (CRC Press, Boca Raton, 2020).

[57] K. T. McDonald, *On the history of the radiation reaction*, 2018, http://kirkmcd.princeton.edu/examples/selfforce.pdf.

[58] P. A. M. Dirac, Classical theory of radiating electrons, Proc. R. Soc. A **167,** 148 (1938).

[59] L. D. Landau and E. Lifshitz, *The Classical Theory of Fields: Volume 2* (Butterworth-Heinemann, London, 1975), vol. 2.

[60] B. S. DeWitt and R. W. Brehme, Radiation damping in a gravitational field, Ann. Phys. (N.Y.) **9,** 220 (1960).

[61] A. Tursunov, M. Kološ, Z. Stuchlík, and D. V. Gal'tsov, Radiation reaction of charged particles orbiting a magnetized schwarzschild black hole, Astrophys. J. **861,** 2 (2018).

[62] H. A. Lorentz, *La théorie électromagnétique de Maxwell et son application aux corps mouvants* (EJ Brill, 1892), Vol. 25, 10.1007/978-94-015-3447-5_4.

[63] K. Destounis and K. D. Kokkotas, Gravitational-wave glitches: Resonant islands and frequency jumps in non-integrable extreme-mass-ratio inspirals, Phys. Rev. D **104,** 064023 (2021).

[64] S. Isoyama, R. Fujita, H. Nakano, N. Sago, and T. Tanaka, Evolution of the Carter constant for resonant inspirals into a

Kerr black hole: I. The scalar case, Prog. Theor. Exp. Phys. **2013**, 063E01 (2013).

[65] S. Isoyama, R. Fujita, H. Nakano, N. Sago, and T. Tanaka, "Flux-balance formulae" for extreme mass-ratio inspirals, Prog. Theor. Exp. Phys. **2019**, 013E01 (2019).

[66] Z. Nasipak and C. R. Evans, Resonant self-force effects in extreme-mass-ratio binaries: A scalar model, Phys. Rev. D **104**, 084011 (2021).

[67] R. Haberman, Energy bounds for the slow capture by a center in sustained resonance, SIAM J. Appl. Math. **43**, 244 (1983).

[68] M. van de Meent, Conditions for sustained orbital resonances in extreme mass ratio inspirals, Phys. Rev. D **89**, 084033 (2014).

[69] The Event Horizon Telescope Collaboration, First M87 event horizon telescope results. VI. The shadow and mass

of the central black hole, Astrophys. J. Lett. **875**, L6 (2019).

[70] The Event Horizon Telescope Collaboration, First M87 event horizon telescope results. VIII. Magnetic field structure near the event horizon, Astrophys. J. Lett. **910**, L13 (2021).

[71] B. Sarkar and S. Das, Standing shocks in magnetized dissipative accretion flow around black holes, J. Astrophys. Astron. **39**, 3 (2018).

[72] M. Del Santo, J. Malzac, R. Belmont, L. Bouchet, and G. De Cesare, The magnetic field in the X-ray corona of Cygnus X-1, Mon. Not. R. Astron. Soc. **430**, 209 (2013).

[73] A. G. Smith and C. M. Will, Force on a static charge outside a Schwarzschild black hole, Phys. Rev. D **22**, 1276 (1980).